

Formic Acid Adsorption on Anatase TiO₂(001)–(1 × 4) Thin Films Studied by NC-AFM and STM[†]

Robert E. Tanner,^{*,‡} Akira Sasahara,[§] Yong Liang,^{||,⊥} Eric I. Altman,[‡] and Hiroshi Onishi[§]

Department of Chemical Engineering, Yale University, P.O. Box 208286, New Haven, Connecticut 06520-8286, Surface Chemistry Laboratory, Kanagawa Academy of Science and Technology, KSP East 404, 3-2-1 Sakado, Takatsu-ku, Kawasaki, Kanagawa 213-0012, Japan, Environmental Molecular Sciences Laboratory, Pacific Northwest National Laboratory, MS K8-93, P.O. Box 999, Richland, Washington 99352, and Motorola Labs, 7700 S. River Parkway, AZ83/ML26, Tempe, Arizona

Received: March 5, 2002; In Final Form: May 16, 2002

Atomic resolution scanning tunneling microscopy (STM), noncontact atomic force microscopy (NC-AFM), X-ray photoemission spectroscopy (XPS), low-energy electron diffraction (LEED), and formic acid adsorption experiments were used to characterize the (001) surface of anatase TiO₂. A combination of NC-AFM and STM imaging was used to distinguish features due to geometrical and electronic effects. The contrast in images of the bare (1 × 4) surface and the formate-covered surface is dominated by the surface topography in both NC-AFM and STM, although electronic effects in the troughs contribute features to the STM images that are absent from NC-AFM images. High-resolution imaging by STM and NC-AFM revealed that the highest point of the ridge of the (1 × 4) structure consists of a single row of atoms. Formate adsorbs at under-coordinated Ti sites in the added rows with a minimum separation of 2a₀ and never adsorbs in the trenches even though the trenches also likely expose under-coordinated Ti atoms. The sticking probability of formate on the anatase TiO₂(001)–(1 × 4) surface is near unity initially, and falls dramatically once the saturation coverage of 1/8 ML is reached. We show that of the current models for the (1 × 4) reconstruction, an added row plus surface oxygen vacancy model and the recently proposed add-molecule model are in best agreement with all of the data.

I. Introduction

As increasing attention has turned to the chemical and physical properties of oxide surfaces, a small number of materials have become favorite “model systems” for study. The choices have been motivated by a wide range of factors, including current commercial application, availability of the material in pure well-characterized form, suitability for ultrahigh vacuum (UHV) study, and potential for future exploitation in novel devices. Among these model systems is titanium dioxide (TiO₂), a material with unique physical and chemical properties including high dielectric constant, excellent optical transmittance in the visible and near-infrared region and high refractive index. The latter explains the traditional role for TiO₂ as a pigment in paint, plastics, paper, foodstuffs, and dentistry. Titania is also being exploited in humidity¹ and gas² sensors, as optical coatings and protective layers on optical fibers,^{3,4} as gate electrodes for metal-oxide semiconductor devices,^{5,6} and as a blood-compatible biomaterial.^{7–9} Furthermore, it was discovered that TiO₂ has potential as a photocatalyst for water cleavage,^{10–13} and there

is also interest in using TiO₂ in catalytic water detoxification^{14,15} and other photocatalytic processes.¹⁶

The anatase polymorph of TiO₂ is generally used in catalytic applications, and it has been reported that nanoparticles of TiO₂ may preferentially adopt the anatase structure despite the lower energy of bulk rutile compared to bulk anatase.¹⁷ Because natural mineral samples are generally small and contain significant levels of impurities, much recent effort has focused on the controlled growth of single-crystal anatase films by molecular beam epitaxy (MBE)¹⁸ and chemical vapor deposition (CVD). Anatase (001) films have been deposited onto SrTiO₃(100)^{18–21} and LaAlO₃(100)²² substrates.

Investigations of rutile have revealed surface reconstructions that are heavily influenced by local stoichiometry, which in turn is controlled by at least three different processes: creation/healing of surface oxygen vacancies, diffusion of interstitial Tiⁿ⁺ (*n* ≤ 3), and diffusion of TiO₂ “moieties”. It has not yet been established whether these mechanisms are also active in anatase TiO₂. During anatase growth, the stoichiometric surface spontaneously forms a two-domain (1 × 4) reconstruction rather than bulk-terminated (1 × 1).^{21,23,24} The driving force and mechanism by which this reconstruction is formed is poorly understood, and the reconstruction’s atomic configuration has not been determined. Several different models have been proposed to date. Some of the first surface studies proposed nonstoichiometric models such as those involving missing rows of oxygen^{23,25} (Figure 1a) or added rows of TiO₃²³ (Figure 1c). On the basis of low-energy electron diffraction (LEED) and angle-resolved mass spectroscopy of recoiled ions, a stoichiometric model was proposed based on surface nanofaceting to

[†] Part of the special issue “John C. Tully Festschrift”.

^{*} To whom correspondence should be addressed. Fax: +1 203 432-4387. Web: www.eng.yale.edu. E-mail: rob.tanner@physics.org. Current address: Department of Physics, University of Warwick, Coventry, CV4 7AL, United Kingdom.

[‡] Department of Chemical Engineering, Yale University.

[§] Surface Chemistry Laboratory, Kanagawa Academy of Science and Technology.

^{||} Environmental Molecular Sciences Laboratory, Pacific Northwest National Laboratory.

[⊥] Motorola Labs.

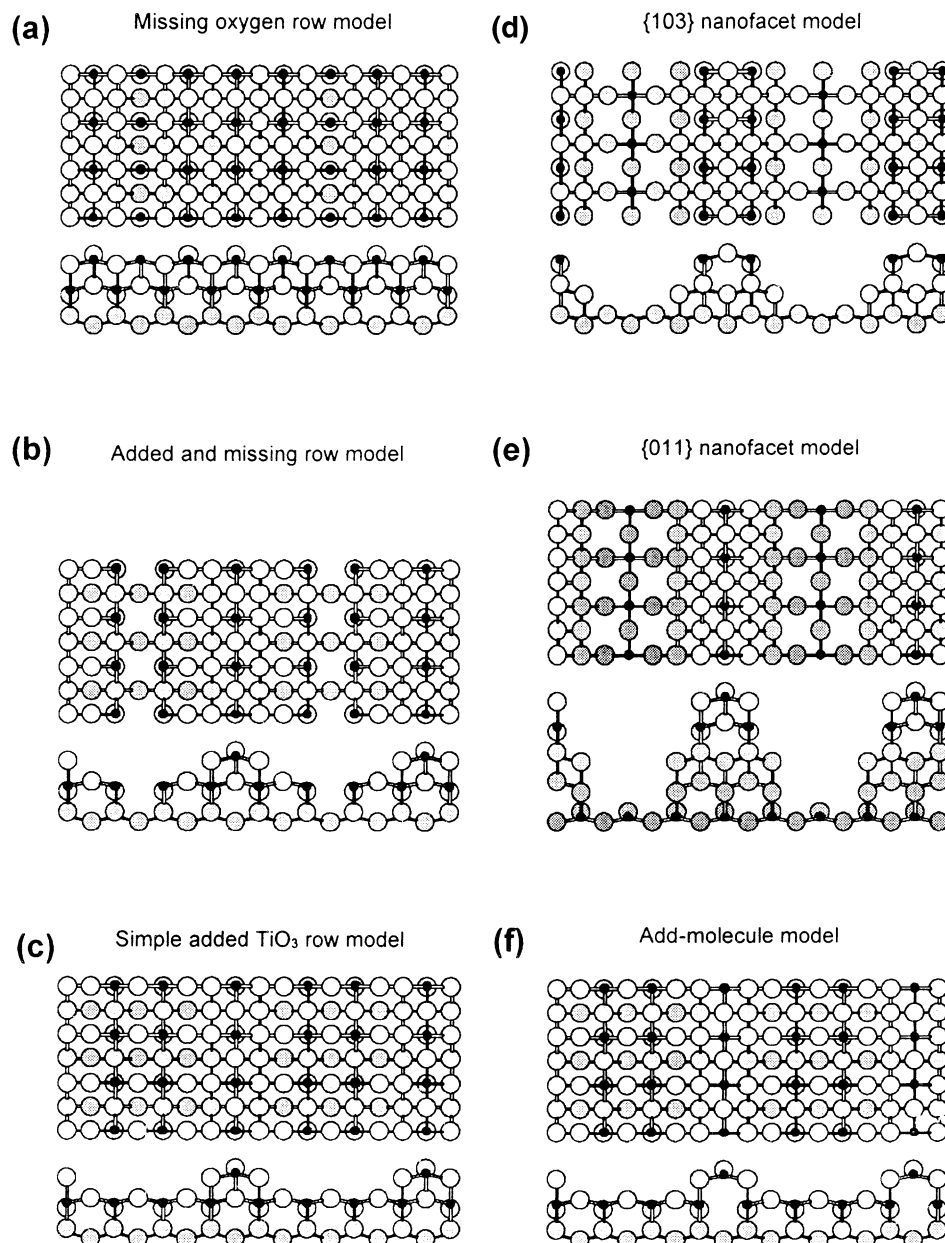


Figure 1. Projections along the [001] direction (upper) and [010] direction (lower) of six models for the anatase (001)–(1×4) reconstruction. The small black spheres represent Ti cations, whereas the larger spheres represent O anions. Heavier shading is used for each successive layer. The atoms are in their unrelaxed bulklike positions. (a) Missing oxygen row model,^{23,25} (b) Liang et al. added and missing row model,²¹ (c) Simple added rows of TiO_3 ,²³ (d) Herman et al. {103} nanofacet model,²³ (e) Tanner et al. {011} nanofacet model,²⁴ and (f) Lazzeri and Selloni add-molecule model.³⁴

form {103} faces²³ (Figure 1d). Scanning tunneling microscopy (STM) images seemed to favor a stoichiometric “added and missing row model”²¹ (Figure 1b), while our group has recently suggested a stoichiometric {011} nanofacet model based on STM and carboxylate adsorption²⁴ (Figure 1e). Photoemission spectroscopy results favor the stoichiometric models.^{21,23,24}

Concurrent theoretical investigations have focused on bulk anatase^{26–29} and (1×1) surfaces.^{29–33} Only one study of the (1×4) reconstruction has been published.³⁴ This first-principles density functional calculation found that a model in which an added TiO_3 molecule replaces a surface oxygen row competes in energy with the (1×1) surface (Figure 1f). The driving force seems to be a lowering of surface energy through stress relaxation.

In this article, we present a scanning probe microscopy (SPM) study of anatase (001)–(1×4) and formic acid adsorption.

Noncontact atomic force microscopy (NC-AFM) was employed to discern the contributions from electronic and topographic effects in STM images. Under-coordinated surface Ti are known to be active for formate adsorption on rutile (110),³⁵ so adsorption of formic acid (HCOOH) and SPM imaging was used here to titrate the active adsorption sites on anatase (001). By locating the adsorption sites in both STM and NC-AFM, the contrast in STM images was determined to be topography-dominated. Analysis of SPM images of bare anatase and formate-covered anatase surfaces allowed us to assess the validity of the different models in the literature. We discuss the different criteria for a good model for the (1×4) reconstruction, and find all sub-stoichiometric and nanofacet models to be deficient in some respect, whereas we find the simple added row plus surface vacancy model and the new add-molecule model to be in best agreement with our data.

II. Experimental Section

(a) Experimental Apparatus. Experiments were carried out using an ultrahigh vacuum (UHV) STM/AFM system (JEOL JSPM4500A) with a base pressure lower than 2.0×10^{-8} Pa. The preparation chamber was equipped with LEED optics, an X-ray photoemission spectrometer (XPS) with a Mg anode, an ion gun for Ar^+ bombardment, leak valves, and a fast-entry lock. A separate imaging chamber contained the noncontact atomic force/scanning tunneling microscope. Using the deflection of laser light from its backside, the cantilever deflection was measured with a four-quadrant optical detector.

(b) Tip and Sample Preparation. Anatase (001) thin films were grown via oxygen-plasma-assisted molecular beam epitaxy (OPA-MBE), at the Pacific Northwest National Laboratory.²¹ Heated 1 wt % Nb-doped $\text{SrTiO}_3(100)$ substrates and slow growth rates were used to improve the film quality. Analysis by XPS and LEED was completed before the samples were removed from the system. The specimens were flown to Japan, where they were either mechanically ground or cleaved to a size of $1 \times 7 \text{ mm}^2$. Each piece was mounted on top of a resistively heated Si wafer and inserted into the vacuum system. The surface was cleaned of adsorbed hydrocarbons by repeated cycles of Ar^+ sputtering (500 eV, $0.7 \mu\text{A}$ sample current, 2 min) and annealing in O_2 (5–10 min) at a temperature of $\sim 750^\circ\text{C}$. The formation of a (1×4) termination was verified with LEED and SPM.

Annealing temperatures were measured by an infrared pyrometer (Minolta TR630). The values quoted in this study are generally higher than those cited in our previous work.²⁴ We believe that the pyrometer consistently overestimated the temperature, due to uncertainties in the appropriate emissivity value ($\epsilon = 0.5$ was assumed here) and the possibility of measuring the temperature of the Si heater through the transparent TiO_2 sample. A thermocouple was used in the prior work.

A conductive Si cantilever (NSCS11, NT-MDT) was used for NC-AFM. It was occasionally sputtered with 500 eV Ar^+ to remove contamination from the tip apex.

(c) Experimental Procedure. A piezoactuator at the fixed end of the Si cantilever was controlled with a constant amplitude ac signal, causing the free end of the cantilever to vibrate at its resonant frequency of 295.4 kHz. The peak-to-peak oscillation was estimated to be $\sim 60 \text{ \AA}$. Forces between the tip and sample cause a slight shift of the tip's vibration frequency. As the tip was rastered across the surface by x - and y -piezoactuators, the tip-sample separation (z) was regulated by a third piezoactuator so as to keep the frequency shift (Δf) constant. Noncontact mode AFM measurements were made at room temperature and the piezoactuators were calibrated to a $\text{Si}(111)-(7 \times 7)$ standard sample. All images are represented as raw data, with no filtering performed other than slope correction and contrast enhancement via manipulation of the gray scale.

Scanning tunneling microscopy images were acquired at room temperature in constant current mode at a tunneling current of 1.0 nA and positive sample biases only (i.e., empty-states imaging).

Formic acid was purified by freeze-pump-thaw cycles until the pressure did not rise above 1.0×10^{-3} Pa. Subsequently the HCOOH vapor was dosed onto the sample at room temperature in the preparation chamber. The dose in Langmuir (L) was calculated from the product of chamber pressure and the exposure time, where 1 L is defined as 1.0×10^{-6} Torr·s.

III. Results

(a) Effect of Surface Treatment on the Anatase $\text{TiO}_2(001)-(1 \times 4)$ Surface. The sample was observed during the preparation stages to monitor the development of the (1×4) structure. In Figure 2, parts a and b, we present NC-AFM images that were recorded following sputtering of the sample with Ar^+ at 500 eV for 2 min, annealing at 720°C in 1.0×10^{-5} Pa of O_2 for 5 min, and cooling in O_2 . Parallel bright rows are visible in some parts of the images, spaced by four times the surface unit cell (16 \AA). The spacing along the rows is not visible in these images; the LEED pattern from this surface indicated that a (1×4) reconstruction had partly formed, and so the periodicity along the rows was equal to \mathbf{a}_0 or 3.78 \AA . The dark spots are due to the cantilever briefly jumping to contact and reflect the difficulty in acquiring images when the surface corrugation amplitude is large.³⁶

Annealing at 750°C in UHV for 5 min improved the surface ordering, revealed in the NC-AFM image in Figure 2, parts c and d. The parallel bright rows appear more ordered and the terrace size has increased. Bright strings are visible in Figure 2, parts c and d, that are located on top of (1×4) reconstructed terraces. The bright strands bridge the (1×4) rows and some are higher with raised portions at each end.

The surface quality was further improved by annealing in UHV at 770°C for 5 min (Figure 2e) with a concomitant improvement in the LEED pattern. An example is presented in Figure 2f.

Annealing rutile $\text{TiO}_2(110)-(1 \times 1)$ in UHV is known to result in the production of both sub-stoichiometric strands³⁷ and other stoichiometric reconstructions based on partial terraces.^{38–40} To quantify the ratio of $\text{Ti}^{4+}:\text{Ti}^{n+}$ in the surface layers following annealing in UHV we carried out XPS measurements, and the results are presented in Figure 2, parts g and h. Previous XPS studies of defect densities on rutile TiO_2 have shown that the $(110)-(1 \times 1)$ surface is fully stoichiometric.⁴¹ We have included data from a rutile $(110)-(1 \times 1)$ sample for comparison, offset for clarity. The rutile surface was first confirmed to be a low-defect (1×1) surface in STM and NC-AFM, the spectrum from anatase is identical with no evidence of lower binding energy shoulders due to reduced Ti. Correspondingly, the signal from O 1s (Figure 2h) shows a single peak due to O^{2-} . Data from both anatase and rutile show satellite peaks $\sim 8.5 \text{ eV}$ lower in binding energy.

(b) Surface Defects. The wide range STM image in Figure 3a shows the anatase (001) surface following ion bombardment, annealing at 680°C in 5×10^{-5} Pa of O_2 (5 min), cooling in O_2 , and annealing in UHV at 750°C (5 min). Small terraces, typically $100\text{--}200 \text{ \AA}$ across are formed that show a predominance of $\langle 100 \rangle$ -type step edges. Frequently, the $\langle 100 \rangle$ step edges are serrated with $3\mathbf{a}_0$ or $4\mathbf{a}_0$ periodicity. Each terrace is patterned with bright rows that show no atomic periodicity at this magnification, but are usually separated by $4\mathbf{a}_0$. Irregularities on the surface include spots centered on the bright rows, kinks where the bright row jogs by \mathbf{a}_0 and anti-phase boundaries (APBs) where a jog of $2\mathbf{a}_0$ forces the row to terminate. Atomic-scale defects in the bright rows are visible in Figure 3b, and are indicated by white arrows. There are instances in Figures 3b, 3d, and 2e where the rows do not conform to the (1×4) periodicity of the LEED pattern. In Figure 2e a local (1×5) structure is produced where the distance between the bright rows is 18.75 \AA ($5\mathbf{a}_0$) in the center of the image. To the lower left, three rows are spaced by only 11.25 \AA ($3\mathbf{a}_0$), equivalent to a local (1×3) structure. The row registry is restored outside the small region between the dotted

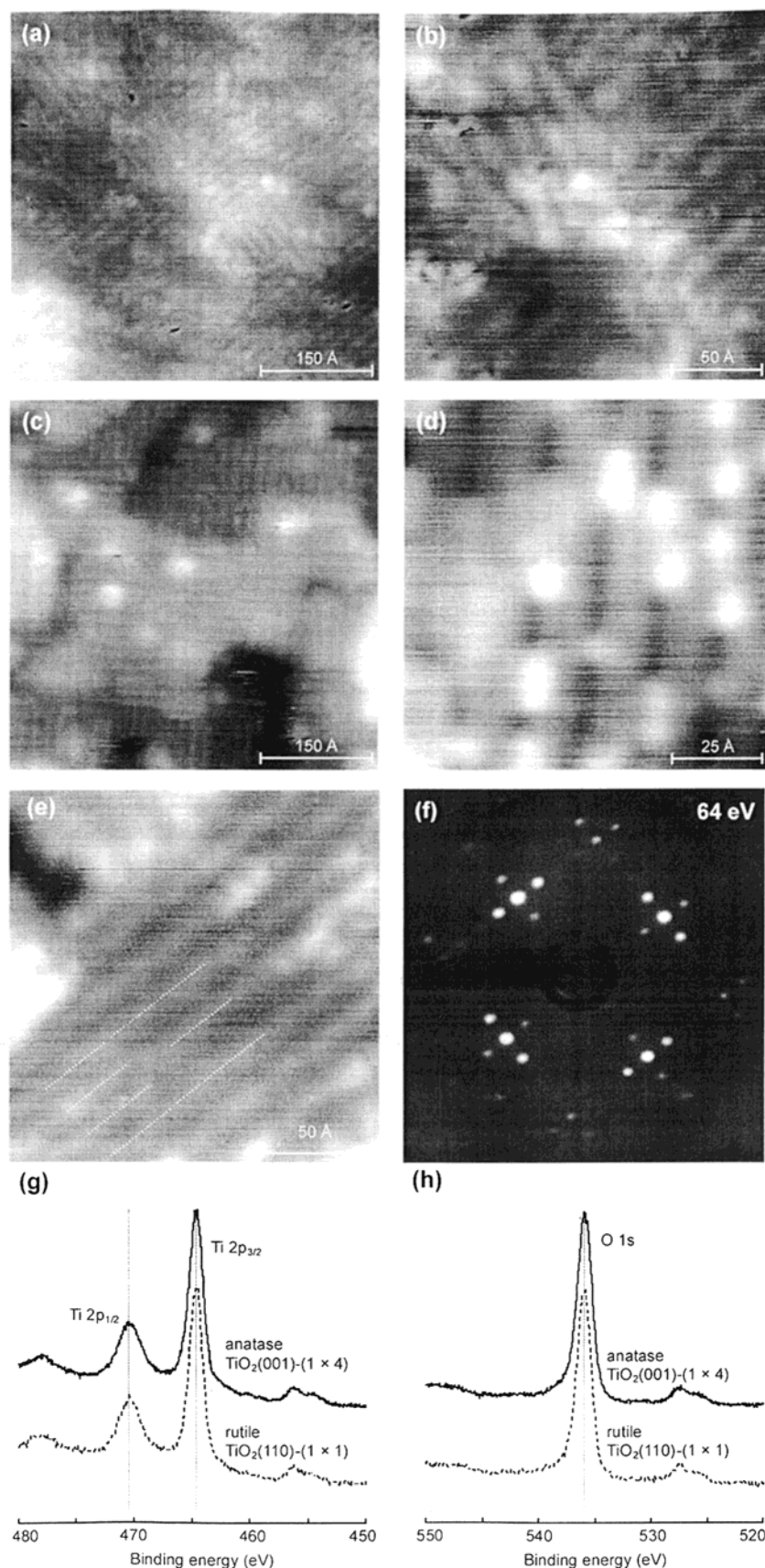


Figure 2. Preparation of the anatase (001)-(1 × 4) surface. (a)-(e) Noncontact AFM images. (a),(b) The incipient (1 × 4) structure is present after ion bombardment at 500 eV, annealing in O₂ at 720 °C, and cooling in O₂. (c),(d) The quality of the surface is improved significantly following UHV annealing at 750 °C, although portions of the undissolved upper terraces remain. (e) Following further annealing 770 °C the NC-AFM images reveal a surface with mostly (1 × 4) ordering although local variation exists, indicated with black lines (3a₀ periodicity) and white lines (5a₀ periodicity). (f) Typical LEED pattern following annealing in UHV. (g),(h) The corresponding XPS data show how the surface layers contain exclusively Ti⁴⁺ cations. No major features distinguish the anatase peak profiles from rutile TiO₂ data. (a) $\Delta f = -266$ Hz, $V_s = +0.90$ V, (b) $\Delta f = -266$ Hz, $V_s = +0.90$ V, (c) $\Delta f = -80$ Hz, $V_s = +0.76$ V, (d) $\Delta f = -77$ Hz, $V_s = +0.76$ V, and (e) $\Delta f = -95$ Hz, $V_s = 0.9$ V.

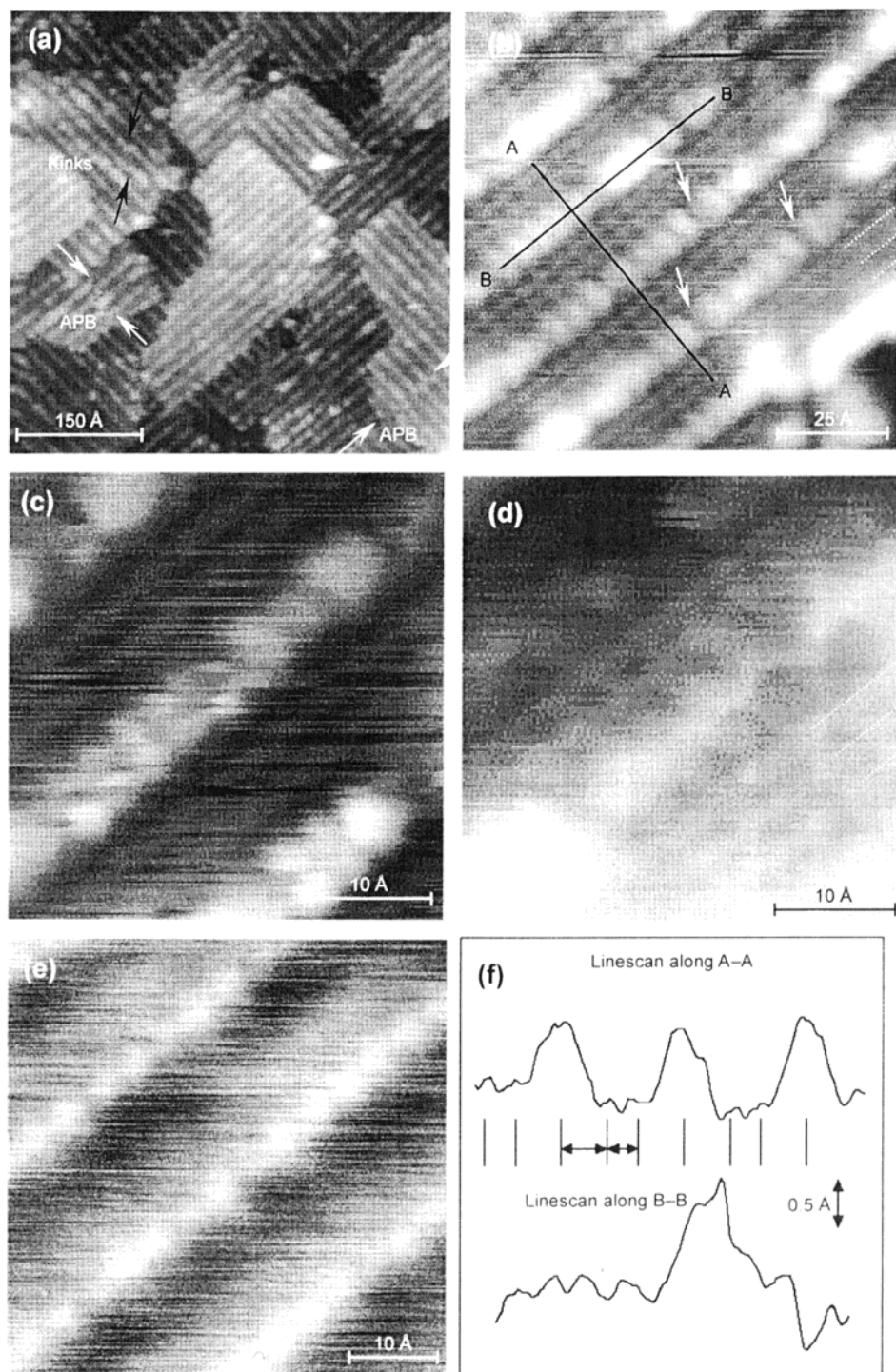


Figure 3. SPM images of the bare anatase (001)-(1 × 4) surface. (a) Wide range STM image following annealing in oxygen and in UHV. Reconstructed step edges run along $\langle 100 \rangle$ directions, black arrow mark rows that contain a kink, and white arrows mark positions of two anti-phase boundaries. (b),(c) High-resolution STM reveals how the bright rows are composed of two parallel rows of bright points and defects. Between the bright rows are two fainter rows. (d) Between the bright rows are three fainter rows where a local (1 × 5) periodicity exists. (e) High-resolution NC-AFM image. (f) Linescans from the image in (b) taken along a line perpendicular to the bright rows (A–A) and parallel to the bright rows (B–B). A tunneling current set point of 1.0 nA was used in (a)–(d). (a) $V_s = +1.0$ V, $I_t = 1.0$ nA, (b) $V_s = +1.0$ V, (c) $V_s = +0.80$ V, (d) $V_s = +1.0$ V, $35 \text{ Å} \times 35 \text{ Å}$, and (e) $\Delta f = -115$ Hz, $V_s = +0.90$ V.

lines. Many other examples of local (1 × 3) and (1 × 5) periodicity were observed in both NC-AFM and STM images, and some are highlighted with dotted lines in Figure 3, parts b and d. In rare cases, (1 × 2) periodicity was also observed.

(c) High-Resolution Imaging of the (1 × 4) Reconstruction. The results of a high-resolution SPM study of the anatase (001)-(1 × 4) reconstruction are also presented in Figure 3. In particular, the different appearance of the surface in STM and

NC-AFM images is considered. In STM images, the bright rows are resolved as separate features elongated perpendicular to the rows (Figure 3b). At yet higher resolution, these are revealed to consist of two parallel rows of bright points (Figure 3c). Between the rows there are pairs of fainter rows (Figure 3, parts b and c). Once more, these are revealed to be composed of two parallel lines of faint spots (Figure 3, parts b and d). At the bottom right of Figure 3d, the row separation is locally $5a_0$

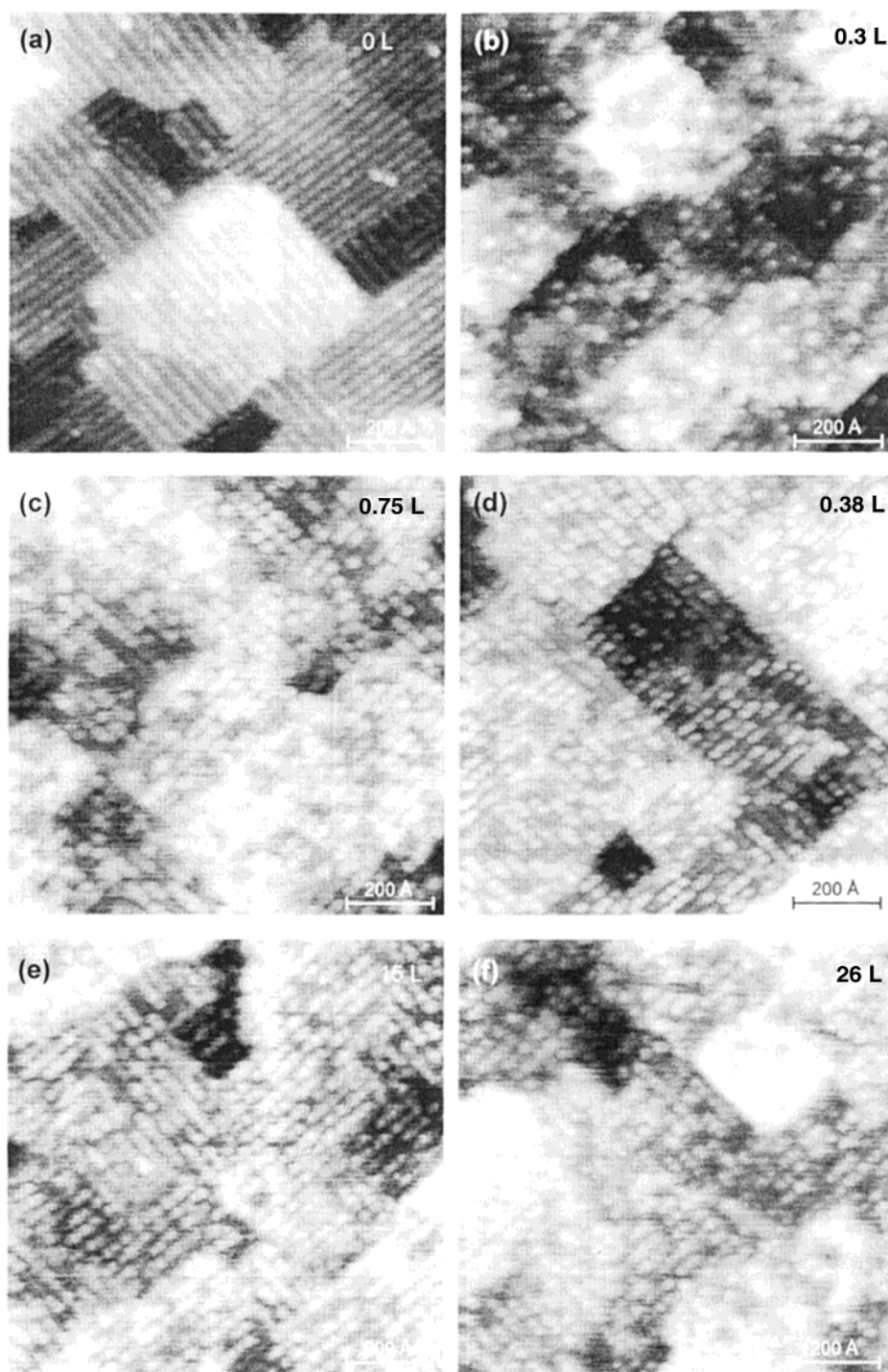


Figure 4. STM images of the anatase (1×4) reconstruction during a sequential dosing experiment. All images were recorded under the conditions $V_s = +1.0$ V, $I_t = 1.0$ nA. The surface was dosed prior to each image, resulting in a cumulative dose of (a) 0 L (clean surface), (b) 0.3 L, (c) 0.75 L, (d) 3.8 L, (e) 15 L, and (f) 26 L.

(another example of local (1×5) periodicity) and three identical rows of faint spots are present. Figure 3f contains linescans from Figure 3b taken along a line perpendicular to the bright rows (A–A) and parallel to the bright rows (B–B), and indicated in Figure 3b.

A comparison of the images by STM in Figure 3c and NC-AFM in Figure 3e are striking. The high-resolution NC-AFM image is significantly different on two counts. First there are no faint strands between the bright rows, and second the crests of the bright rows are composed of single rows of bright points.

(d) Scanning Probe Microscopy of the Adsorption and Reaction of Formic Acid on Anatase $\text{TiO}_2(001)$. The results

of a sequential dosing experiment in which STM images were obtained after repeated doses of formic acid (HCOOH) to the anatase surface are presented in Figure 4. The cumulative dose is shown at the top right of each image. As the surface was dosed with formic acid at room temperature, the appearance of the surface changed from typical clean flat terraces with a small number of defects (Figure 4a) to a surface covered in small bright points (Figure 4, parts b–f). The concentration of bright spots between the images in Figure 4, parts a, b and c, increased with increasing dose. After 0.75 L, however, the density of the bright spots did not increase significantly with further exposure, and even after 26 L, the surface is not completely saturated

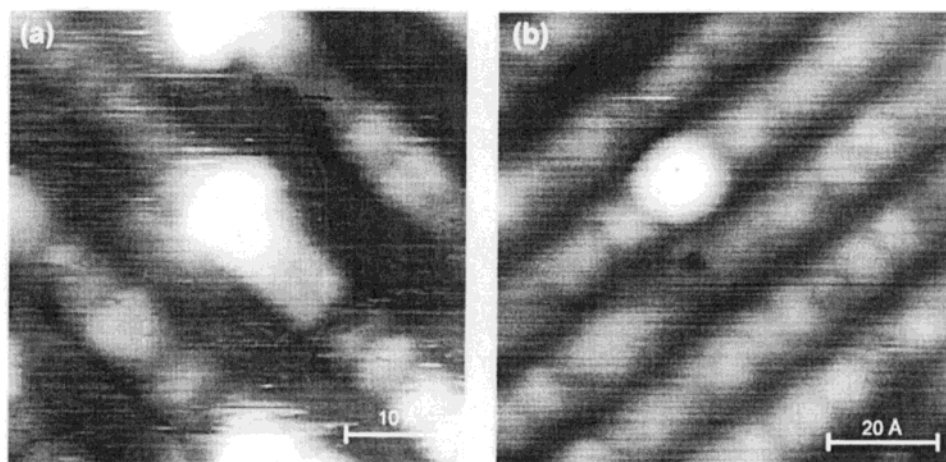


Figure 5. SPM images of submonolayer coverage HCOOH on the anatase (001)-(1 × 4) surface. (a) High-resolution STM image of two formate adsorbates after the surface was exposed to 0.2 L of HCOOH. (b) High-resolution NC-AFM of a single formate adsorbate after exposure to 0.09 L of HCOOH. The images were recorded under the following conditions: (a) $V_s = +0.80$ V, $I_t = 1.0$ nA, and (b) $\Delta f = -30$ Hz, $V_s = +0.50$ V.

with bright spots. The closest proximity of the spots along the rows is 7.5 \AA ($2a_0$). As in our previous work,²⁴ the maximum density of bright spots perpendicular to the rows is 16 \AA ($4a_0$), and there is no evidence for the bright spots between the underlying bright rows of the anatase (1 × 4) surface. At high coverage, the STM images contain features due to the bright spots and steps between substrate terraces only; it became impossible to discern the detail of the (1 × 4) periodicity on the underlying anatase surface.

To identify the location of the bright points, we exposed a clean surface to submonolayer coverages of HCOOH and performed high-resolution STM and NC-AFM. Bright points are aligned with the bright row of the underlying anatase (1 × 4) structure in Figure 5, parts a and b. Note that in the STM image (Figure 5a) the underlying bright rows are also sharply resolved as in Figure 3c. The two new bright points in Figure 5a consist of ovals that are elongated perpendicular to the underlying row and span the width of the bright row. The center of the oval spots is usually aligned with the individual spots of the underlying bright rows. The apparent heights of the bright adsorbates in STM varied between 2 and 3 Å. Even in STM images with a high density of bright points (e.g., Figure 4, parts e and f), linescans showed that the apparent height of the bright points was not constant across the image.

The NC-AFM image in Figure 5b also shows the bright spot atop the bright ridge. The bright spots have an apparent height of the of $\sim 1 \text{ \AA}$ compared to the bright rows.

IV. Discussion

(a) Surface Treatment. Ion bombardment preferentially removes oxygen from transition metal oxide (TMO) surfaces⁴² and, hence, is essentially a tool for surface reduction. In previous work,²⁴ we verified this to be the case, with Ti^{3+} peaks appearing in XPS data from sputtered surfaces, and Ti^{4+} restored as the unique peak after annealing in O_2 . The SPM images presented here obtained after annealing and cooling in O_2 , however, revealed a surface with only short-range order. Our initial supposition—that poor surface ordering could be identified with sub-stoichiometry—was therefore flawed, and we discovered that subsequent annealing in UHV (i.e., exposure to reducing conditions) improved the surface quality. This would suggest that the surface was in fact “over-oxidized” through our attempts to maintain a stoichiometric surface. The XPS data (Figure 2,

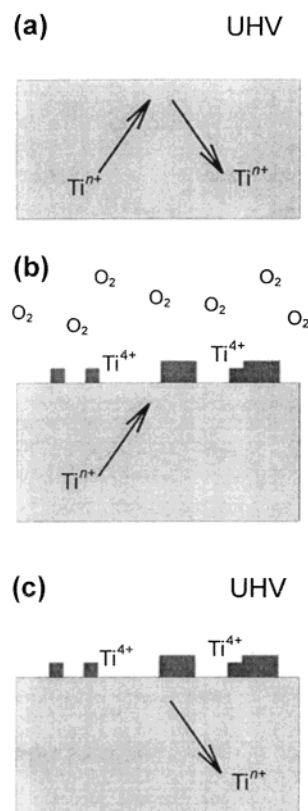


Figure 6. Mechanism for surface structure formation via bulk migration of interstitial Ti^{n+} ($n \leq 3$). (a) Ti^{n+} migrates at an enhanced rate during annealing. (b) Under the oxidizing conditions of an O_2 ambient, the Ti^{n+} is oxidized and trapped at the surface. (c) Under the reducing conditions of UHV annealing, the surface Ti^{4+} is reduced to Ti^{n+} that migrates back into bulk.

parts g and h) unambiguously show that the surface was entirely populated by Ti^{4+} species, even after reduction by annealing at 770°C in vacuum. We conclude that the surface participates in a bulk-assisted surface oxidation/reduction mechanism, similar to that seen in other TMOs including rutile TiO_2 ^{42–44} and $\text{WO}_3(001)$.⁴⁵ Sputtering generates surface Ti^{n+} species ($n \leq 3$), that are relatively mobile and can diffuse into the bulk (Figure 6a). In an oxidizing ambient interstitial Ti^{n+} is trapped at the surface, forming a stoichiometric but disordered surface (Figure 6b). Mild reduction by heating in UHV reduces

some of the rough TiO_2 formed at the surface to liberate oxygen and allow Ti^{n+} to diffuse back into the bulk (Figure 6c). Although this process requires net reduction of the TiO_2 crystal, the sub-stoichiometry is accommodated by bulk reduction and the (1×4) reconstructed surface remains fully oxidized, as borne out in the XPS data of Figure 2, parts g and h, and elsewhere.^{19,21,24} We expect that increasing the O_2 annealing time would also result in a smooth surface as the small TiO_2 islands formed by segregation coarsen with time, while increasing the O_2 annealing temperature would increase the mobility of the newly formed TiO_2 moieties — also leading to a smoother surface. Such effects have been observed for rutile.⁴⁰

The bright strings in the NC-AFM images of Figure 2, parts c and d, are also a consequence of the bulk-assisted reduction mechanism. These strings are left where the disordered upper terraces are not completely incorporated into a stoichiometric terrace or dissolved into the bulk. NC-AFM images do not contain contributions from electronic tunneling into empty states at the end of rows (cf., STM of added rows on $\text{TiO}_2(110)$ ⁴⁶), so we assign the bright patches on the strands to topographical distortion resulting from stress relaxation at a free end, assuming that in this image the NC-AFM tip–surface interaction does not significantly contain effects due to electrostatic effects.

The oxidation state of the surface cations is an important tool in the evaluation of models for the (1×4) reconstruction: the absence of Ti^{3+} allows us to eliminate all models based on nonstoichiometric surface reconstructions (Figure 1, parts a and c). Furthermore, 6-fold and 5-fold coordinated Ti may exist at Ti^{4+} centers, but Ti^{4+} in crystalline solids strongly favors an octahedral over a tetrahedral environment, so the occurrence of 4-fold coordinated Ti in the bulk is rare.⁴⁷ At the surface, under coordinated Ti (5-fold or 4-fold) tend to produce a surface with a high energy, and reconstruction to increase coordination is frequently observed.

(b) Defects in the (1×4) Reconstructed Surface. The atomic-scale faint spots in STM images of the (001) surface (Figure 3a) were not visible in the NC-AFM, so we identify them with electronic features of the surface. These may be caused by a surface or subsurface defect, such as a cation vacancy where the local density of states (LDOS) is perturbed. We might expect these points to be important for the adsorption of formate, since coordinatively unsaturated sites (cus) are well-known as catalytically reactive sites. Heightened catalytic activity may also be anticipated at the ends of bright strands (Figure 2d), at kinks, at APBs, and at reconstructed step edges. Similar features have been observed at [001] step edges on rutile $\text{TiO}_2(110)$ ⁴¹ and we speculate that a similar serration may be responsible on the anatase $\text{TiO}_2(001)$ surface.

The identification of surface defect structures at the atomic scale and larger, and the local variation in row periodicity from $2a_0$ to $5a_0$ are important observations that provide further structural criteria to be satisfied by a plausible model.

(c) STM and NC-AFM at High Resolution. From linescans across STM images (e.g., Figure 3), we find the same periodicity in the bright rows (B–B) and in the double faint rows (not shown). Across the rows, the separation of 15.9 \AA confirms the $4\times$ periodicity. The faint rows in the trenches are 4.1 \AA apart, slightly larger than the value of a_0 (3.78 \AA). This may be due to surface relaxation, or a feature in the electronic density of states that is not necessarily representative of the precise local topography. Within the bright rows, the dark and bright points

may be a consequence of an atomic-scale defect such as the enhanced LDOS around a missing O anion or changed oxidation state in the vicinity of a Ti vacancy, or of an adsorbed species.

The high-resolution STM and NC-AFM images (Figure 3, parts c and e, respectively) both show bright rows that are $\sim 16 \text{ \AA}$ apart separated by dark trenches. In constant-current STM images the apparent height difference between the dark and light parts of the image is influenced by a combination of topographic and electronic contributions. Using the additional bright spots after HCOOH adsorption as markers (Figure 5) we see that the bright rows in the STM correspond to the same bright rows in NC-AFM. Therefore, the contrast in STM is at least partly due to topographic features on the anatase surface. Hence, the bright rows in both STM and NC-AFM images correspond to physical protrusions.

The detail between and within each of the bright rows, however, is strongly dependent on the imaging technique. In the STM images of Figure 3, parts b and c, the troughs between the bright rows contain two fainter rows, first observed by Liang et al.²¹ Because these features are absent from the NC-AFM image, we identify these dark lines as an electronic feature. Within the bright rows, the NC-AFM image (Figure 3e) shows that the row crest is composed of a single bright feature. On the other hand, the STM images show broader row crests, and in Figure 3c we succeeded in resolving the crests as due to two separate features.

The image in Figure 3e appears asymmetric about the bright rows. However, the darkest part of the image does not consistently lie to one side of the bright row, and on other occasions we recorded images that showed symmetrical rows at similar magnification. Therefore, this apparent asymmetry is attributed to the condition of the tip, and may be influenced by the tip's finite size and the relatively large corrugation amplitude of the surface.

These results shed important light on the structure of the bright rows. The NC-AFM images conclusively show that the row crests are composed of a single row of atoms spaced by a_0 . The STM images may indicate that the rows are straddled by pairs of atoms with high LDOS, or alternatively that the row crests contain single atoms with high LDOS but that certain tip states allow the separate atomic orbitals of these atoms to be resolved.

(d) SPM of Formate on Anatase (001). Because the number of the bright spots in SPM images of the surface initially increased with the formic acid dose, the bright spots can be assigned to chemisorbed formate (HCOO^-). Although hydrogen is also produced by the dissociative adsorption of formic acid, the hydrogen presumably attaches to bridging oxygen sites to form a hydroxyl species, or alternatively may intercalate into the bulk. The size of the hydroxyl is small compared to the formate, so the large protrusions in NC-AFM images following exposure can be attributed to the formate. As these features appear in the same positions in NC-AFM and STM images, the protrusions in the STM images can also be assigned to formate.

The room-temperature sticking-coefficient for formate at low coverage is near unity. By 0.75 L however, the sticking coefficient falls dramatically, since the surface is covered with a maximum packing of just $1/8 \text{ ML}$ (0.13 ML) in an idealized (2×4) arrangement. In fact, local packing defects mean that the total coverage is lower than 0.13 ML and that the ordering of the formate overlayer is poor. There is neither evidence for multilayer adsorption, nor for formate attachment in trenches between the (1×4) bright rows. This maximum coverage is

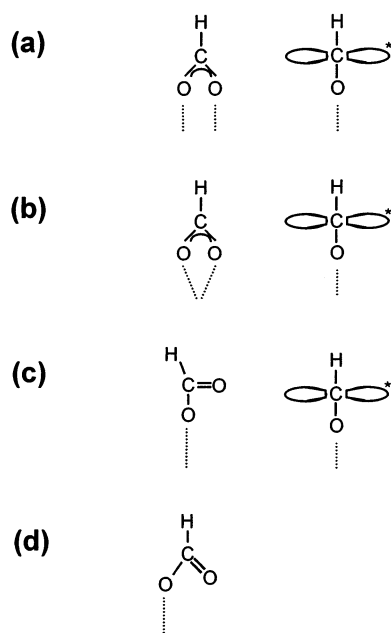


Figure 7. Adsorption geometries for formate on TiO_2 : (a) bridging, (b) bidendate, (c) monodendate, and (d) asymmetric bridge. In (a)–(c) two views rotated 90° are provided.

much lower than on rutile $\text{TiO}_2(110)$, demonstrating that there are no suitable adsorption sites in the trenches.

It is unsurprising that the apparent height of the formate was not the same in STM and NC-AFM images, as the tunnel current and atomic force depend on the tip–surface distance in different ways. The force pulling the tip into the surface is less sensitive to the gap width than the tunneling current, especially when chemically stable molecules cover the surface.⁴⁹ However, the bright spots appear atop the bright rows of the substrate in both STM and NC-AFM, so the contrast in STM images of the adsorbates is dominated by topography and not electronic effects.

(e) Adsorbate Geometry. Formate is generally considered to bond to surfaces in three different ways: (i) bridging bidendate (Figure 7a); (ii) bidendate (Figure 7b); and (iii) monodendate (Figure 7c). Formate adsorption on rutile (110) has been studied in great detail and a consensus has been reached that formate adsorbs in two distinct bridging bidendate configurations.^{35,50–56} In the first, formate bridges adjacent 5-fold coordinated Ti^{4+} along the [001] direction, whereas in the latter formate bonds to a Ti atom exposed by a missing bridging oxygen and a 5-fold Ti exposed as part of the stoichiometric surface. In unoccupied state STM images the adsorbed formate appears as an oval elongated perpendicular to the molecular plane.³⁵ This appearance has been attributed to tunneling into the lowest unoccupied molecular orbital (LUMO) of the molecule that extends perpendicular to the molecular plane as shown in Figure 7. We recently showed²⁴ that adsorbed formate displays a similar shape on anatase (001): in this case, the features were elongated parallel to the $4\times$ direction of the reconstruction. Further, the molecules were never closer than $2a_0$ apart, and so it was suggested that formate also bonds to anatase (001) in a bridging bidendate manner. Although the results presented here show exactly the same features, the STM images also revealed that the bright features associated with formate do not appear centered between the maxima along the top of the reconstruction ridges as shown in Figure 5a. Because the maxima in STM images of TiO_2 surfaces are generally

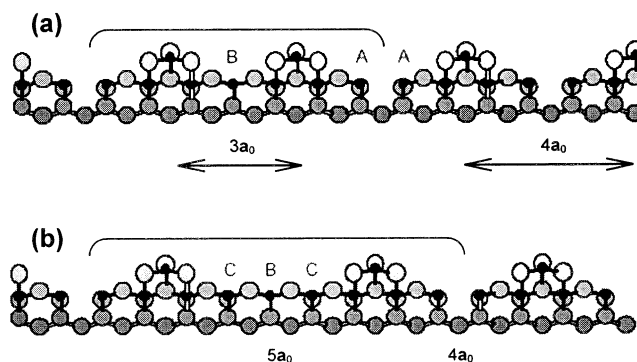


Figure 8. Schematic diagram of the added and missing row model. (a) To create the local (1×3) periodicity, a trench between the bright rows is eliminated, removing “A”-type sites and introducing “B”-type sites. (b) To create the local (1×5) periodicity, a trench between the bright rows is widened, introducing both “B”- and “C”-type sites. The same conventions on atom labeling as used as in Figure 1.

associated with the Ti atoms, this observation is not consistent with a bridging bidendate configuration.

It is difficult to rationalize the results in terms of the bidendate and monodendate configurations in Figure 7, parts b and c. First, neither configuration precludes the molecules from being closer than $2a_0$ apart. The bidendate configuration also requires exposed 4-fold coordinated Ti. We previously showed that the reconstructed anatase (001) surface is not active for bimolecular ketonization reactions that are enabled by 4-fold coordinated Ti^{4+} .²⁴ Further, the row structure of the reconstruction suggests bridging oxygens between the Ti atoms at the top of the ridges. This dictates that a Ti atom at the top of the ridge with two accessible dangling bonds, or missing ligands, would have to have these bonds oriented perpendicular to the ridge. This would cause the molecules to appear elongated *parallel* to the bright rows, the *opposite* of what is observed. The monodendate configuration would allow the molecules to rotate freely and so the molecules would appear symmetric.

In recent infrared work on formate adsorbed on anatase powders, an asymmetric formate was reported in which one of the formate oxygens forms a strong bond to a surface Ti atom, whereas the other bonds more weakly to the surface.⁵⁷ This can take the form of the asymmetric bridge configuration pictured in Figure 7d. In comparison to the rutile surface, such a structure may be more favorable here because the distance between the Ti atoms is 3.8 \AA on anatase (001) versus 3.0 and 3.6 \AA for the two bridging configurations on rutile (110). This structure can explain the observed orientation of the molecule, the minimum $2a_0$ separation, and the registry of the molecules with the substrate.

(f) Current Models for the (1×4) Reconstruction. The data and discussion from the previous sections allow us to evaluate the different atomic models proposed for the (1×4) structure.

The model based on $\{103\}$ nanofacets contains many exposed 4-fold coordinated Ti sites. The high energy of such sites is likely to result in substantial atomic relaxation into the surface to produce a more stable structure, where the atoms are shielded from the surface. Even if these sites were stable, it is unlikely that formate would bind symmetrically atop the ridges as seen in the SPM images. As shown in Figure 1d, the oxygen atoms buckle outward between the Ti atoms on either side of the ridge and inward along the ridge and so it would be more likely that formate would bridge Ti atoms along the side of the ridge. Also, if formate could bridge such a ridge, this would align the molecule perpendicular to the ridge which would cause it to

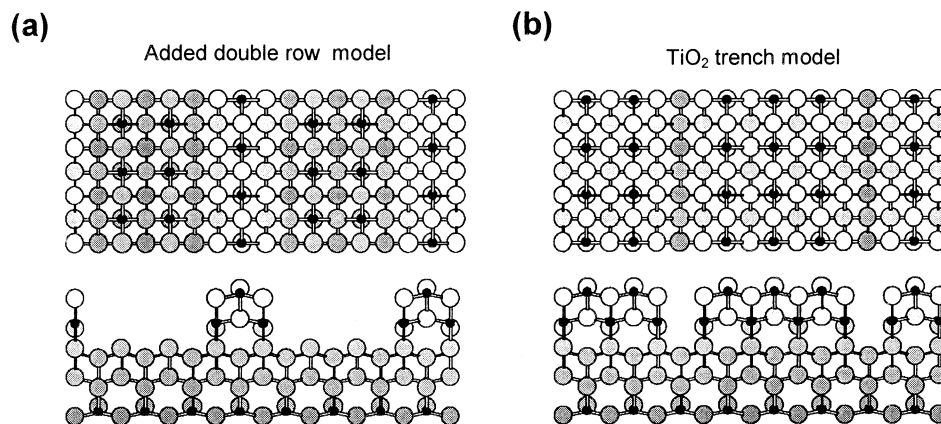


Figure 9. Projections along the [001] direction (upper) and [010] direction (lower) of two stoichiometric models that are based on {011} faceting. The atoms are in their unrelaxed bulklike positions. (a) Added double row model, and (b) TiO_2 trench model. The same conventions on atom labeling as used as in Figure 1.

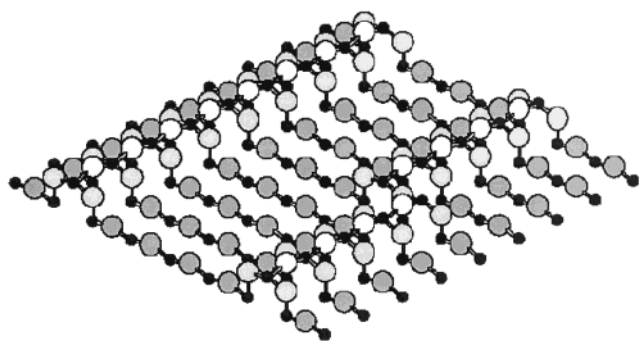


Figure 10. How the change of periodicity may occur via a kink in the simple added row model or add-molecule model. The same conventions on atom labeling as used as in Figure 1.

appear elongated perpendicular to the row, and would not preclude an \mathbf{a}_0 separation between neighboring adsorbates. Thus, the images of adsorbed formate are not consistent with the {103} nanofacet model. In addition, if STM preferentially imaged electronic features in the trenches, then the 5-fold Ti sites would produce only one line between the bright rows, rather than two as seen in STM images.

The added and missing row model is also flawed because it provides 4-fold coordinated Ti as possible adsorption sites in the trenches, where no formate molecules are seen in SPM images. It is also impossible to accommodate (1×3) and (1×5) without introducing features that would have dramatically different contrast in STM. Figure 8 illustrates the way that type “B” and “C” sites have a substantially different atomic environment. In STM, these would appear very differently from the normal type “A” sites. In particular, the “A”-type sites are missing 2-fold coordinated outward buckled oxygens, while 3-fold coordinated inward buckled oxygens are missing at the “B”-type and “C”-type sites.

The XPS data show that the surface layers contain Ti in the 4+ oxidation state alone, so it would seem that models based on local nonstoichiometry—the missing O row model and the simple added TiO_3 row model—are not suitable. However, the simple added TiO_3 row could be valid, provided $1/3$ ML oxygen is removed from the surface. This would maintain TiO_2 stoichiometry and would explain why the formate layer adsorbs in a partially disordered state (Figure 4). However, we are not confident that the surface could support such a high density of oxygen vacancies, and it is not clear why this model would lower in energy than an unreconstructed (1×1) termination.

The {011} nanofacet model was proposed based on two experimental observations: (i) that the {011} planes form the lowest energy anatase surfaces; and (ii) that the reconstructed anatase surface is not active for reactions associated with 4-fold coordinated Ti^{4+} .²⁴ As illustrated in Figure 1e, {011} faceting exposes only 5-fold coordinated Ti atoms. The model in Figure 1e is just one realization of a {011} nanofaceted surface, in this case with the facet planes two unit cells long. If the facet planes are a single unit cell long, then the model can be pictured as a double added row structure (Figure 9a), a stoichiometric structure that can readily accommodate (1×3) and (1×5) periodicities. The model also places exposed 5-fold coordinated Ti atoms at the top of the ridge that can account for the location of the adsorbates. The primary difficulty with the model is that it predicts at least a half unit cell high corrugation, roughly a factor of 2 greater than what is seen in both the STM and NC-AFM images. Another stoichiometric variation based on double-height steps consists of trenches where units of TiO_2 are missing (Figure 9b). Without substantial relaxation however, this model does not accurately reproduce the contrast difference in SPM images between the troughs and the crests of the rows. We are currently performing calculations to evaluate the magnitude of the relaxation effects, and to compare the relative stability of the models depicted in Figure 1 and Figure 9.

Therefore, we are left with the newly proposed add-molecule model. This is very similar to the simple added TiO_3 row model, but avoids being over-stoichiometric by the inclusion of an oxygen vacancy row *beneath* the added row (cf., in the center of the plane for the added and missing row model). The subsequent relaxation of the atoms is thought to stabilize this structure.³⁴ This model can explain many of the features that we have observed. The added rows appear bright in both STM and NC-AFM images, as required, and local changes in surface periodicity may be accomplished via a kink or jog, as depicted in Figure 10. The bright spots in NC-AFM are the O atoms at the crest of the added row. It is not possible to determine unequivocally whether the bright spots in STM images are due to tunneling into orbitals on the under-coordinated 4-fold Ti atoms.

Despite this apparent good agreement, the presence of 4-fold Ti^{4+} would appear to be a problem with the ad-molecule model. In our recent work on the chemistry of adsorbed formate and acetate,²⁴ we saw no evidence of bimolecular ketonization products that have been associated with 4-fold coordinated Ti^{4+} .^{24,58–61} These pathways, however, require the Ti atom to bind two carboxylates. If the Ti atom in the ad-molecule is

considered to be in a distorted octahedral environment, then Figure 1f shows that the Ti atoms are missing ligands directly above and below the Ti atoms. The latter site is obviously inaccessible and therefore, although the Ti atom is 4-fold coordinated it can only bind a single carboxylate and, thus, is incapable of catalyzing bimolecular reactions. Supporting this picture, the contours of integrated local density of states in the conduction band for the add-molecule model (Figure 2 of ref 34) show that the unoccupied states associated with the add-molecule are concentrated directly above and below the Ti atom.³⁴ Thus, the (1×4) reconstruction can create unique sites that have no analogues on rutile surfaces. This helps explain why, in contrast to rutile surfaces, formate and acetate adsorbed on anatase (001)– (1×4) are very strongly held and only undergo unselective decomposition at high temperatures.²⁴

Understanding the lack of reactivity of the 5-fold coordinated sites in the trough remains a challenge for all of the proposed models because these are the reactive sites on rutile surfaces. Again though, the contours of integrated local density of states in the conduction band for the ad-molecule model provide insight into this issue.³⁴ The relaxations due to creating the surface and the reconstruction compress the (1×1) section of the surface in the troughs pushing the 2-fold coordinated oxygens outward.^{33,34} The effect is to move the neighboring Ti atoms slightly below the surface and markedly reduce the density of unoccupied states above the Ti atoms, particularly in comparison to the Ti atoms on the ridges. Because these are the states that the carboxylates bind to, we can understand why the molecules bond so much more strongly to the ridges. Although, these calculations applied to the add-molecule model, similar effects can be expected in other models.

V. Conclusions

We have studied the (1×4) reconstructed surface of thin film anatase (001) and of the surface exposed to formic acid vapor by LEED, XPS, and high-resolution NC-AFM and STM. Formation of the anatase (001)– (1×4) reconstruction is governed by a mechanism of bulk-reduction, whereby interstitial Ti^{3+} species are produced and surface Ti^{4+} is eliminated. Following UHV annealing the surface forms a regular (1×4) periodicity that is occasionally broken by a local (1×3) or (1×5) pattern.

The room-temperature sticking coefficient of formate on anatase $TiO_2(001)$ – (1×4) is near unity up to the saturation coverage of 0.13 ML, after which it falls dramatically. The formate molecules are observed as protrusions atop bright substrate rows in both STM and NC-AFM images and are not observed in the trenches between the substrate bright rows. The position of the formate adsorbates allows us to identify unambiguously that the ridges in STM and NC-AFM images are both due to the topographic effects of atomic reordering.

From X-ray photoelectron spectra we are able to exclude stoichiometric models, and SPM images show that models based on nanofaceting are unsuitable. The recently proposed ad-molecule model is consistent with our data. Formate adsorbs at the 4-fold coordinated Ti in the ad-molecules, and does not adsorb at 5-fold coordinated sites in the trough. These results reveal important difference between the chemical reactivity of the anatase surface compared to rutile (110) where 5-fold coordinated sites are active, and reveal strong dependence of activity on surface atomic structure.

Acknowledgment. The authors are grateful to H. Uetsuka for assistance with experiments and A. Selloni for useful

discussions. Financial assistance for one of us (R.E.T.) from the Marubun Research Promotion Foundation is gratefully acknowledged. This work was supported by the US Department of Energy Basic Energy Sciences program, under Grant No. DE-FG02-98ER14882. Research at PNNL was performed in the Environmental Molecular Sciences Laboratory, a national scientific user facility sponsored by the Department of Energy's Office of Biological and Environmental Research.

References and Notes

- (1) Gusmano, G.; Montesperelli, G.; Nunziante, P.; Traversa, E.; Montenero, A.; Braghini, M.; Mattogno, G.; Bearzotti, A. Humidity-Sensitive Properties of Titania Films Prepared using the Sol–Gel Process. *J. Ceram. Soc. Jpn.* **1993**, *101*, 1095–1100.
- (2) Huusko, J.; Lantto, V.; Torvela, H. TiO_2 Thick-Film Gas Sensors and Their Suitability for $NO_{(x)}$ Monitoring. *Sens. Actuators B* **1993**, *16*, 245–248.
- (3) Yeung, K. S.; Lam, Y. W. A Simple Chemical Vapor-Deposition Method for Depositing Thin TiO_2 Films. *Thin Solid Films* **1983**, *109*, 169–178.
- (4) Jurek, K.; Guglielmi, M.; Kuncova, G.; Renner, O.; Lukes, F.; Navratil, M.; Krousky, E.; Vorlicek, V.; Kokesova, K. Characterization of TiO_2 and ZrO_2 Coatings on Silica Slabs and Fibres. *J. Mater. Sci.* **1992**, *27*, 2549–2555.
- (5) Brown, W. D.; Grannemann, W. W. C-V Characteristics of Metal-Titanium Dioxide-Silicon Capacitors. *Solid State Electron.* **1978**, *21*, 837–846.
- (6) Kingon, A. I.; Maria, J. P.; Streiffer, S. K. Alternative Dielectrics to Silicon Dioxide for Memory and Logic Devices. *Nature* **2000**, *406*, 1032–1038.
- (7) Ebert, R.; Schaldach, M. *Proceedings of the World Congress on Medical Physics and Biomedical Engineering, Hamburg 1982* 3.07.
- (8) Huang, N.; Chen, Y. R.; Luo, J. M.; Li, J.; Lu, R.; Xiao, J.; Xue, Z. N.; Liu, X. H. In-Vitro Investigation of Blood Compatibility of Titanium with Oxide Layers of Rutile Structure. *J. Biomater. Appl.* **1994**, *8*, 404–412.
- (9) Wang, X. H.; Zhang, F.; Li, C. R.; Zheng, Z. H.; Wang, X.; Liu, X. H.; Chen, A. Q.; Jiang, Z. B. Improvement of Blood Compatibility of Artificial Heart Valves via Titanium Oxide Film Coated on Low-Temperature Isotropic Carbon. *Surf. Coat. Technol.* **2000**, *128*, 36–42.
- (10) Fujishima, A.; Honda, K. Electrochemical Photolysis of Water at a Semiconductor Electrode. *Nature* **1972**, *238*, 37–38.
- (11) O'Regan, B.; Grätzel, M. A Low-Cost, High-Efficiency Solar-Cell based on Dye-Sensitized Colloidal TiO_2 Films. *Nature* **1991**, *353*, 737–740.
- (12) Butter, M. A.; Ginley, D. S. Review: Principles of Photoelectrochemical Solar Energy Conversion. *J. Mater. Sci.* **1980**, *15*, 1–19.
- (13) Kavan, L.; Grätzel, M.; Gilbert, S. E.; Klemenz, C.; Scheel, H. J. Electrochemical and Photoelectrochemical Investigation of Single-Crystal Anatase. *J. Am. Chem. Soc.* **1996**, *118*, 6716–6723.
- (14) Choi, W. Y.; Termin, A.; Hoffmann, M. R. The Role of Metal-Ion Dopants in Quantum-Sized TiO_2 —Correlation between Photoreactivity and Charge-Carrier Recombination Dynamics. *J. Phys. Chem.* **1994**, *98*, 13 669–13 679.
- (15) Choi, W. Y.; Termin, A.; Hoffmann, M. R. Effects of Metal-Ion Dopants on the Photocatalytic Reactivity of Quantum-Sized TiO_2 Particles. *Angew. Chemie* **1994**, *33*, 1091–1092.
- (16) Oak Ridge National Laboratories report: *EPA Site Program Demonstration of a TiO_2 Photocatalytic Oxidation Technology on the SW-31 Spring at the East Tennessee Technology Park (ETTP), Oak Ridge, Tennessee*, <http://www.ornl.gov/K25/techdemo/epasite.htm>.
- (17) Remillard, J. T.; McBride, J. R.; Nietering, K. E.; Drews, A. R.; Zhang, X. Real Time in situ Spectroscopic Ellipsometry Studies of the Photocatalytic Oxidation of Stearic Acid on Titania Films. *J. Phys. Chem. B* **2000**, *104*, 4440–4447.
- (18) Zhang, H.; Banfield, J. F. Thermodynamic Analysis of Phase Stability of Nanocrystalline Titania. *J. Mater. Chem.* **1998**, *8*, 2073–2076.
- (19) Chambers, S. A. Epitaxial Growth and Properties of Thin Film Oxides. *Surf. Sci. Rep.* **2000**, *39*, 105–180.
- (20) Herman, G. S.; Gao, Y.; Tran, T. T.; Osterwalder, J. X-ray Photoelectron Diffraction Study of an Anatase Thin Film: $TiO_2(001)$. *Surf. Sci.* **2000**, *447*, 201–211.
- (21) Gao, Y.; Herman, G. S. Growth of Epitaxial Anatase (001) and (101) Films. *Thin Solid Films* **2001**, *397*, 157–161.
- (22) Liang, Y.; Gan, S.; Chambers, S. A.; Altman, E. I. Surface Structures of Anatase $TiO_2(001)$: Reconstruction, Atomic Steps, and Domains. *Phys. Rev. B* **2001**, *63*, 5402.
- (23) Murakami, M.; Matsumoto, Y.; Nakajima, K.; Makino, T.; Segawa, Y.; Chikyow, T.; Ahmet, P.; Kawasaki, M.; Koinuma, H. Anatase TiO_2 Thin Films Grown on Lattice-Matched $LaAlO_3$ Substrate by Laser Molecular-Beam Epitaxy. *Appl. Phys. Lett.* **2001**, *78*, 2664–2666.

- (23) Herman, G. S.; Sievers, M. R.; Gao, Y. Structure Determination of the Two-Domain (1×4) Anatase $\text{TiO}_2(001)$ Surface. *Phys. Rev. Lett.* **2000**, *84*, 3354–3357.
- (24) Tanner, R. E.; Liang, Y.; Altman, E. I. Structure and Chemical Reactivity of Adsorbed Carboxylic Acids on Anatase $\text{TiO}_2(001)$. *Surf. Sci.* **2002**, *506*, 251–271.
- (25) Hengerer, R.; Bolliger, B.; Erbudak, M.; Grätzel, M. Structure and Stability of the Anatase $\text{TiO}_2(101)$ and (001) Surfaces. *Surf. Sci.* **2000**, *460*, 162–169.
- (26) Fahmi, A.; Minot, C.; Silvi, B.; Causá, M. Theoretical Analysis of the Structures of Titanium Dioxide Crystals. *Phys. Rev. B* **1993**, *47*, 11 717–11 724.
- (27) Stashans, A.; Lunell, S.; Bergström, R.; Hagfeldt, A.; Lindquist, S.-E. Theoretical Study of Lithium Intercalation in Rutile and Anatase. *Phys. Rev. B* **1996**, *53*, 159–170.
- (28) Stashans, A.; Lunell, S.; Grimes, R. W. Theoretical Study of Lithium Perfect and Defective TiO_2 Crystals. *J. Phys. Chem. Solids* **1996**, *9*, 1293–1301.
- (29) Beltrán, A.; Sambrano, J. R.; Calatayud, M.; Sensato, F. R.; Andrés, J. Static Simulation of Bulk and Selected Surfaces of Anatase TiO_2 . *Surf. Sci.* **2001**, *490*, 116–124.
- (30) Fahmi, A.; Minot, C. A Theoretical Investigation of Water Adsorption in Titanium Dioxide Surfaces. *Surf. Sci.* **1994**, *304*, 343–359.
- (31) Oliver, P. M.; Watson, G. W.; Kelsey, E. T.; Parker, S. C. Atomistic Simulation of the Surface Structure of the TiO_2 Polymorphs Rutile and Anatase. *J. Mater. Chem.* **1997**, *7*, 563–568.
- (32) Vittadini, A.; Selloni, A.; Rotzinger, F. P.; Grätzel, M. Structure and Energetics of Water Adsorbed at TiO_2 Anatase (101) and (001) Surfaces. *Phys. Rev. Lett.* **1998**, *81*, 2954–2957.
- (33) Lazzeri, M.; Vittadini, A.; Selloni, A. Structure and Energetics of Stoichiometric TiO_2 Anatase Surfaces. *Phys. Rev. B* **2001**, *63*, 5409.
- (34) Lazzeri, M.; Selloni, A. Stress-Driven Reconstruction of an Oxide Surface: The Anatase $\text{TiO}_2(001)-(1 \times 4)$ Surface. *Phys. Rev. Lett.* **2001**, *87*, 6105–+.
- (35) Onishi, H.; Iwasawa, Y. STM Imaging of Formate Intermediates Adsorbed on a $\text{TiO}_2(110)$ Surface. *Chem. Phys. Lett.* **1994**, *226*, 111–114.
- (36) Kobayashi, K.; Yamada, H.; Horiuchi, T.; Matsushige, K. Investigations of C_{60} Molecules Deposited on $\text{Si}(111)$ by Noncontact Atomic Force Microscopy. *Appl. Surf. Sci.* **1999**, *140*, 281–286.
- (37) Onishi, H.; Fukui, K.; Iwasawa, Y. Atomic-Scale Surface Structures of $\text{TiO}_2(110)$ Determined by Scanning Tunneling Microscopy—A New Surface-Limited Phase of Titanium Oxide. *Bull. Chem. Soc. Jpn.* **1995**, *68*, 2447–2458.
- (38) Pang, C. L.; Haycock, S. A.; Raza, H.; Murray, P. W.; Thornton, G.; Gülsören, O.; James, R.; Bullet, D. W. Added Row Model of $\text{TiO}_2(110)-(1 \times 2)$. *Phys. Rev. B* **1998**, *58*, 1586–1589.
- (39) Bennett, R. A.; Stone, P.; Price, N. J.; Bowker, M. *Phys. Rev. Lett.* **1999**, *82*, 3831–3834. Two (1×2) Reconstructions of $\text{TiO}_2(110)$: Surface Rearrangement and Reactivity Studies using Elevated Temperature Scanning Tunneling Microscopy.
- (40) Li, M.; Hebenstreit, W.; Gross, L.; Diebold, U.; Henderson, M. A.; Jennison, D. R.; Schultz, P. A.; Sears, M. P. Oxygen-Induced Restructuring of the $\text{TiO}_2(110)$ Surface: A Comprehensive Study. *Surf. Sci.* **1999**, *437*, 173–190.
- (41) Wang, L.-Q.; Baer, D. R.; Engelhard, M. H. Creation of Variable Concentrations of Defects on $\text{TiO}_2(110)$ using Low-Density Electron-Beams. *Surf. Sci.* **1994**, *320*, 295–306.
- (42) Henderson, M. A. Mechanism for the Bulk-Assisted Reoxidation of Ion Sputtered TiO_2 Surfaces: Diffusion of Oxygen to the Surface or Titanium to the Bulk? *Surf. Sci.* **1995**, *343*, L1156–L1160.
- (43) Onishi, H.; Iwasawa, Y. Dynamic Visualisation of a Metal Oxide Surface/Gas-Phase Reaction: Time-Resolved Observation by Scanning Tunneling Microscopy at 800 K. *Phys. Rev. Lett.* **1996**, *76*, 791–794.
- (44) Onishi, H.; Iwasawa, Y. STM Observation of Surface Reactions on a Metal Oxide. *Surf. Sci.* **1996**, *357/358*, 773–776.
- (45) Tanner, R. E.; Altman, E. I. Effect of Surface Treatment on the $\gamma\text{-WO}_3(001)$ Surface: A Comprehensive Study of Oxidation and Reduction by Scanning Tunneling Microscopy and Low-Energy Electron Diffraction. *J. Vac. Sci. Technol. A* **2001**, *19*, 1502–1509.
- (46) Tanner, R. E.; Castell, M. R.; Briggs, G. A. D. High-Resolution Scanning Tunneling Microscopy of the Rutile $\text{TiO}_2(110)$ Surface. *Surf. Sci.* **1998**, *412–413*, 672–681.
- (47) Cotton, F. A.; Wilkinson, G. *Advanced Inorganic Chemistry*, 5th ed.; John Wiley and Sons: New York, 1998.
- (48) Diebold, U.; Lehman, J.; Mahmoud, T.; Kuhn, M.; Leonardelli, G.; Hebenstreit, W.; Schmidt, M.; Varga, P. Intrinsic Defects on the $\text{TiO}_2(110)-(1 \times 1)$ Surface and their Reaction with Oxygen: A Scanning Tunneling Microscopy Study. *Surf. Sci.* **1998**, *411*, 137–153.
- (49) Onishi, H.; Sasahara, A.; Uetsuka, H.; Ishibashi, T. Molecule-Dependent Topography Determined by Noncontact Atomic Force Microscopy: Carboxylates on $\text{TiO}_2(110)$. *Appl. Surf. Sci.* **2002**, in press.
- (50) Fukui, K.-I.; Onishi, H.; Iwasawa, Y. Imaging of Individual Formate Ions Adsorbed on $\text{TiO}_2(110)$ Surface by Noncontact Atomic Force Microscopy. *Chem. Phys. Lett.* **1997**, *280*, 296–301.
- (51) Sasahara, A.; Uetsuka, H.; Onishi, H. NC-AFM Topography of HCOO and CH_3COO Molecules Coadsorbed on $\text{TiO}_2(110)$. *Appl. Phys. A* **2001**, *72*, S101–S103.
- (52) Fukui, K.; Onishi, H.; Iwasawa, Y. Atom-Resolved Image of the $\text{TiO}_2(110)$ Surface by Noncontact Atomic Force Microscopy. *Phys. Rev. Lett.* **1997**, *79*, 4202–4205.
- (53) Bennett, R. A.; Stone, P.; Smith, R. D.; Bowker, M. Formic Acid Adsorption and Decomposition on Nonstoichiometric $\text{TiO}_2(110)$. *Surf. Sci.* **2000**, *454–456*, 390–395.
- (54) Cocks, I. D.; Guo, Q.; Patel, R.; Williams, E. M.; Román, E.; de Segovia, J. L. The Structure of $\text{TiO}_2(110)-(1 \times 1)$ and $-(1 \times 2)$ Surfaces with Acetic Acid Adsorption—A PES Study. *Surf. Sci.* **1997**, *377–379*, 135–139.
- (55) Hayden, B. E.; King, A.; Newton, M. A. Fourier Transform Reflection—Absorption IR Spectroscopy Study of Formate Adsorption on $\text{TiO}_2(110)$. *J. Phys. Chem. B* **1999**, *103*, 203–208.
- (56) Gutiérrez-Sosa, A.; Martínez-Escobedo, P.; Raza, H.; Lindsay, R.; Wincott, P. L.; Thornton, G. Orientation of Carboxylates on $\text{TiO}_2(110)$. *Surf. Sci.* **2001**, *471*, 163–169.
- (57) Popova, G. Y.; Andrushkevich, T. V.; Chesalov, Y. A.; Stoyanov, E. S. In situ FTIR Study of the Adsorption of Formaldehyde, Formic Acid, and Methyl Formate at the Surface of TiO_2 (Anatase). *Kinetics and Catalysis* **2000**, *41*, 805–811.
- (58) Kim, K. S.; Barteau, M. A. Pathways for Carboxylic Acid Decomposition on TiO_2 . *Langmuir* **1988**, *4*, 945–953.
- (59) Kim, K. S.; Barteau, M. A. Structural Dependence of the Selectivity of Formic Acid Decomposition on Faceted $\text{TiO}_2(001)$ Surfaces. *Langmuir* **1990**, *6*, 1485–1488.
- (60) Kim, K. S.; Barteau, M. A. Structure and Composition Requirements for Deoxygenation, Dehydration and Ketonisation Reactions of Carboxylic Acids on $\text{TiO}_2(001)$ Single-Crystal Surfaces. *J. Catal.* **1990**, *125*, 353–375.
- (61) Idriss, H.; Lusvardi, V. S.; Barteau, M. A. Two Routes to Formaldehyde from Formic Acid on $\text{TiO}_2(001)$ Surfaces. *Surf. Sci.* **1996**, *348*, 39–48.